

# Synthesis and Photoluminescence of Cd-doped $\alpha$ -MnS Nanowires

Dae Sung Kim, Jin Young Lee, Chan Woong Na, Sang Won Yoon, Shin Young Kim, and Jeunghye Park\*

Department of Chemistry, Korea University, Jochiwon 339-700, Korea

Younghun Jo and Myung-Hwa Jung

Quantum Material Research Team, Korea Basic Science Institute, Daejeon 305-333, Korea

Received: June 25, 2006; In Final Form: July 28, 2006

Cd-doped  $\alpha$ -MnS nanowires (av diam = 70 nm) were synthesized by the chemical vapor deposition of MnCl<sub>2</sub>/CdS powders. They all consisted of single-crystalline rock-salt MnS structures with the [111] growth direction. The X-ray diffraction pattern analysis indicates that 10% Cd doping would expand the lattice constants by 0.3%. As the content of Cd increases, the band edge emission band (2.9 eV) of photoluminescence becomes broader, and the Mn<sup>2+</sup> emission band (1.6 eV), which emerged at temperatures below  $\sim 150$  K, decreases in intensity. The decay time of the 1.6 eV band decreases from 40 to 30  $\mu$ s when the Cd doping is increased from 0 to 10%. In contrast to the bulk ( $T_N = 150$  K), the MnS nanowires were found to be paramagnetic with antiferromagnetic interactions. These distinctive magnetic properties of the nanowires have a strong correlation with their photoluminescence, which could be influenced by the nanosize effect and the Cd doping.

## 1. Introduction

In the past few years, one-dimensional (1-D) nanostructures have attracted considerable attention, because of both their fundamental importance and their wide range of technological applications in nanodevices.<sup>1–4</sup> Semiconductor nanowires (NWs) are especially attractive building blocks for assembling active and integrated nanodevice systems. Manganese sulfide (MnS) is an important magnetic semiconductor material [its band gap energy ( $E_g$ ) is 3.2 eV at room temperature],<sup>5</sup> having considerable potential in short wavelength optoelectronic devices. The green  $\alpha$ -MnS (rock-salt structure) is antiferromagnetic with a Néel temperature ( $T_N$ )  $\approx 150$  K.<sup>6–19</sup> It undergoes a lattice contraction at temperatures below  $T_N$  due to rhombohedral or trigonal distortion. It is known that metastable  $\beta$ -MnS (zinc blende structure) and  $\gamma$ -MnS (wurtzite structure) can be irreversibly transformed into  $\alpha$ -MnS by heating.<sup>19–23</sup> Stimulated by the novel properties of nanoscale materials, MnS nanoparticles/nanorods have previously been synthesized using solvothermal and sol–gel reactions.<sup>24–30</sup> Lately, the synthesis of MnS NWs was performed using hydrothermal and chemical vapor deposition (CVD) methods.<sup>31–33</sup> However, controlling the structure and chemical composition of the MnS nanostructures remains a significant challenge.

In this study, we synthesized exclusively single-crystalline Cd ( $\leq 10\%$ )-doped  $\alpha$ -MnS NWs, with a controlled Cd content, by the chemical vapor deposition method. The magnetic and optical properties of Cd-doped  $\alpha$ -MnS bulk crystals have previously been investigated,<sup>15,16</sup> but no studies have so far been reported for their nanostructures. In the bulk crystal, 10% Cd doping results in a decrease of  $T_N$  from 152 to 127 K and a decrease in the decay rate of the photoluminescence. Herein, we investigated the photoluminescence and magnetic properties of Cd-doped  $\alpha$ -MnS NWs, which could be dependent on the

Cd content. The present work is a part of our continuous studies on the Cd<sub>1–x</sub>Mn<sub>x</sub>S NWs system,<sup>34</sup> designed to provide valuable information on how the properties of the NW structure can differ from those of the bulk counterparts.

## 2. Experimental Section

MnCl<sub>2</sub> (99.99%, Aldrich) and CdS (99.99%, Aldrich) powders were placed separately inside a quartz tube reactor. A silicon substrate coated with a 0.01 M ethanol solution of HAuCl<sub>4</sub>·3H<sub>2</sub>O (98+%, Sigma) was positioned at a distance of 10 cm from the Cd source. Argon gas was allowed to flow while the temperature of the reactor was raised or lowered. The temperatures of the Mn and Cd sources and that of the substrates were set at 600–700, 800, and 600 °C, respectively, during the synthesis under argon ambient. The temperature of MnCl<sub>2</sub> was varied in order to control the relative ratio of Mn and Cd in the NW products. Scanning electron microscopy (SEM, Hitachi S-4300), field-emission transmission electron microscopy (TEM, JEOL JEM 2100F and FEI TECNAI G<sup>2</sup> 200 kV), high-voltage TEM (JEOL JEM ARM 1300S, 1.25 MV), electron diffraction (ED), and energy-dispersive X-ray fluorescence (EDX) were employed to examine the morphology and structure of the products. High-resolution X-ray diffraction (XRD) was performed using the 3C2 ( $\lambda = 1.5402$  Å) and 8C2 beam lines ( $\lambda = 1.54520$  Å) of the Pohang light source (PLS) with monochromatic radiation, and the Cu K $\alpha$  line ( $\lambda = 1.5406$  Å) of a laboratory-based diffractometer (Philips X'Pert PRO MRD). X-ray photoelectron spectroscopy (XPS) measurements were obtained at the 8A1 (Undulator U7) beam line of the PLS and also using a laboratory-based spectrometer (VG Scientific ESCALAB 250, Al K $\alpha$  1486.6 eV). The temperature-dependent steady-state photoluminescence (PL) measurements were carried out using an He–Cd laser ( $\lambda = 325$  nm) as the excitation source. The laser power was less than 100 kW/cm<sup>2</sup>. The time-resolved PL spectrum was recorded using an ns-pulse Nd:YAG laser ( $\lambda = 266$  or 355 nm, Coherent Surelite). The magnetic properties

\* To whom correspondence should be addressed: parkjh@korea.ac.kr.

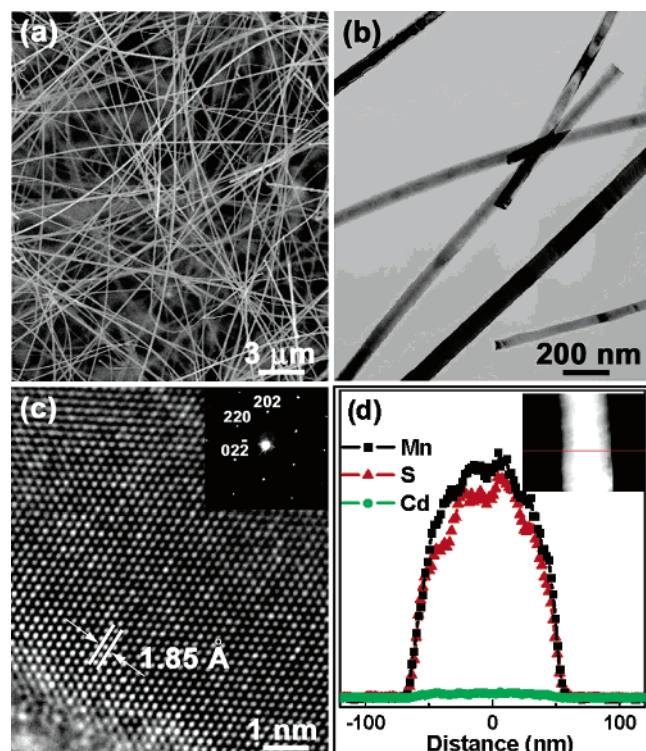


**Figure 1.** (a) SEM micrograph for the high-density MnS NWs grown on the substrate. (b) TEM image showing the typical morphology of the MnS NWs. Their average diameter is 70 nm. (c) Atomic-resolved image reveals highly crystalline lattice planes. The inset corresponds to the SAED pattern, showing the [110] growth direction. (d) Line-scanned EDX shows the negligible Cd content in the MnS NWs.

of the NWs were studied by means of a superconducting quantum interference device (SQUID, Quantum Design) magnetometer.

### 3. Results and Discussion

The SEM micrograph shows that high-density MnS NWs with a length of about 20  $\mu\text{m}$  were grown homogeneously over a large area of the substrates (Figure 1a). The TEM image shows the general morphology of the NWs; most of them are straight and their average diameter is 70 nm (Figure 1b). The atomic-resolved image reveals defect-free lattice planes (Figure 1c). The inset of Figure 1c displays the corresponding selected-area ED (SAED) pattern of the NW, showing the single-crystalline face-centered cubic (fcc) MnS crystal grown with the [110] direction parallel to the long axis. The (220) fringes perpendicular to the growth direction are separated by about 1.85  $\text{\AA}$ , which is close to that of  $\alpha$ -MnS crystal ( $a = 5.224 \text{ \AA}$ ; JCPDS No. 06-0518). The EDX line-scanning profile reveals a 1:1 ratio of Mn:S with a negligible amount ( $<1\%$ ) of Cd  $[(\text{Cd})/(\text{Mn}) + [\text{Cd}]]$ , for the individual MnS NWs (Figure 1d). No oxygen peaks were detected from the NWs.

Figure 2 corresponds to the SEM micrograph of the MnS NW sample containing 5% Cd. The TEM image shows their straight wire morphology with an average diameter of 80 nm (Figure 2b). They have a smooth surface without any overlayers. The EDX line-scanning profile reveals that the 5% Cd is distributed homogeneously along the cross section of the MnS NWs (Figure 2c). The 10% Cd-doped MnS NWs were also synthesized with a high yield. The TEM image shows that the surface of the NWs is less smooth than that of the MnS NWs and 5% Cd-doped MnS NWs (Figure 2d). Their diameter is in the narrow range of 40–60 nm, with an average value of 50

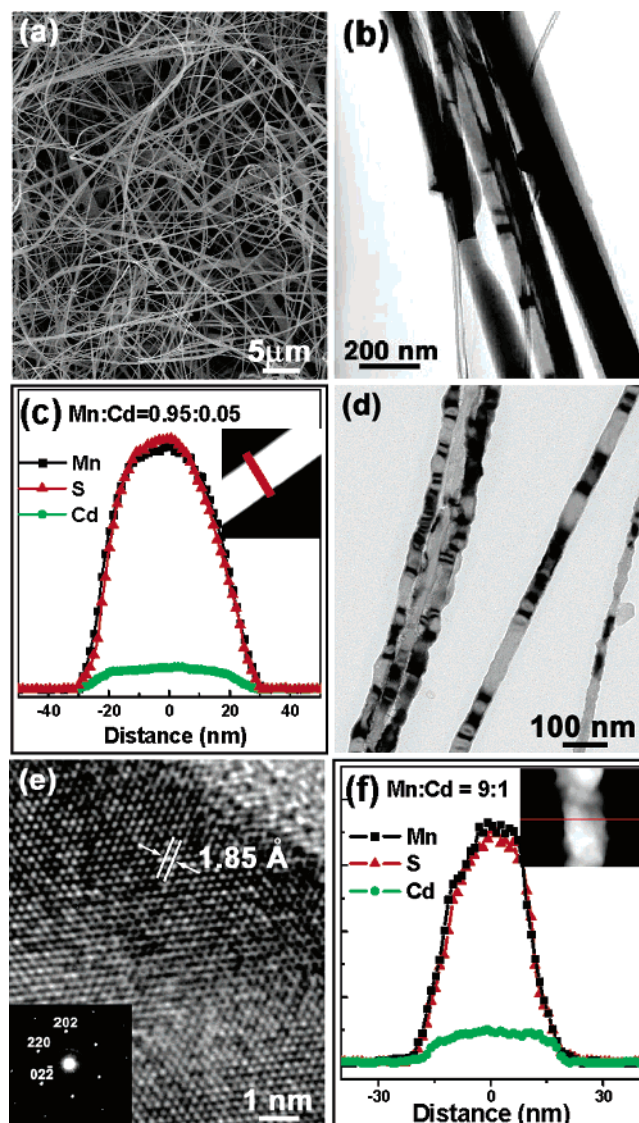


**Figure 2.** (a) SEM micrograph for the high-density 5% Cd-doped MnS NWs grown on the substrate. (b) TEM image showing the smooth surface and an average diameter of 80 nm. (c) Line-scanned EDX shows 5% Cd composition in individual MnS NW. (d) TEM image of 10%-doped MnS NWs, showing the rough surface and an average diameter of 50 nm. (e) Atomic-resolved image reveals highly crystalline lattice planes. The inset corresponds to the SAED pattern, showing the [110] growth direction. (f) Line-scanned EDX shows that the 10% Cd element is homogeneously distributed over the cross section of the MnS NWs.

nm. The atomic-resolved TEM image reveals negligible defects in the lattice planes, despite their rough surface (Figure 2e). The inset shows the SAED pattern, confirming that the single-crystalline MnS crystal grew along the [110] direction. The (220) fringes are separated by 1.85  $\text{\AA}$ . The EDX line-scanning profile reveals that the 10% Cd dopant is homogeneously distributed over the cross section of the MnS NWs (Figure 2f). We observed that all of these MnS NWs consist of single-crystalline cubic MnS nanocrystals grown uniformly along the [110] direction.

The XRD pattern taken from these three different MnS NW samples is displayed with that of commercial MnS (Aldrich, 99.9%) microcrystal size powders, confirming that only cubic  $\alpha$ -MnS crystals were formed (Figure 3a). As the Cd content increases, the peak width becomes slightly broader and the peak position shifts to a lower angle. In the case of 10% Cd doping, the position of the (111) peak is shifted to a lower angle by  $\Delta(2\theta) = 0.1^\circ$  (inset). This suggests that the lattice constant



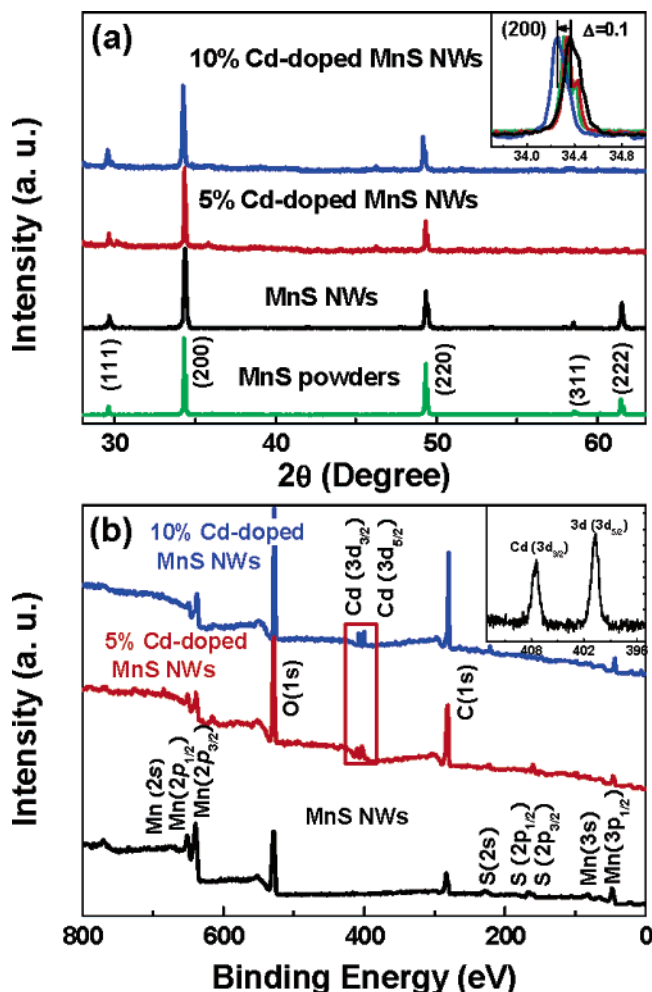


**Figure 3.** (a) XRD patterns of the MnS powders, MnS NWs, and Cd-doped MnS NWs. The inset represents an enlarged-scale (200) peak. (b) XPS survey scans of the MnS NWs and Cd-doped MnS NWs. The inset represents the fine-scanned Cd 3d peaks.

would be expanded by 0.3%. This expansion is probably related to the larger radius of the  $\text{Cd}^{2+}$  (109 pm) ions substituting for the  $\text{Mn}^{2+}$  ions (97 pm) at the octahedral sites of the rock-salt structure. Figure 3b shows the XPS survey scan spectrum of the three MnS NW samples obtained using a photon energy of 1486.6 eV. There are no other elements except for C and O contaminants. No Cd peaks are detected from the MnS NWs (containing <1% Cd from EDX). The Cd-doped NWs show additional Cd peaks whose positions are consistent with those of the reference. The compositions of the 5 and 10% Cd-doped MnS NWs are found to be  $\text{Mn}:\text{Cd} = \sim 95:5$  and  $\text{Mn}:\text{Cd} = \sim 9:1$ , respectively. These percentages are the same as the EDX data, indicating that the Cd is homogeneously doped over the whole NWs. The finely scanned  $\text{In}2p_{3/2}$  and  $\text{In}2p_{1/2}$  peaks of the 10% Cd-doped MnS NWs are shown in the inset.

Part a and b of Figure 4 show the PL spectra of the MnS and 10%-Cd doped MnS NWs, respectively, measured in the temperature range of 7–300 K. The excitation photon energy is 3.815 eV. There is a broad emission band centered at 2.9 eV, which is similar to the band gap of the bulk.<sup>5,31</sup> Thus, we assign it to the band-edge emission band involving the excited states ( $^4\text{T}_1$ ,  $^4\text{T}_2$ ,  $^4\text{A}_1$ , etc.) of the  $\text{Mn}^{2+}$  ions.<sup>5</sup> The other band centered at around 1.6 eV completely vanishes at temperatures above  $\sim 150$  K. This band originates from the decay of the impurity-perturbed excited states of the  $\text{Mn}^{2+}$  ions, generated via the usual d–d energy transfer from the higher excited

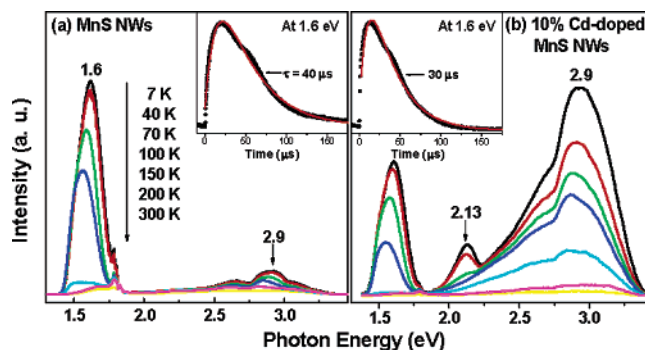


**Figure 4.** Temperature-dependent PL spectrum of the (a) MnS NWs and (b) 10% Cd-doped MnS NWs measured in the temperature range of 7–300 K. The excitation wavelength is 325 nm (3.815 eV) from a He–Cd laser. The insets correspond to the time-resolved spectrum of the 1.6 eV emission band, excited by an Nd:YAG 266 nm (4.66 eV) laser.

states.<sup>17</sup> As the Cd content increases, the band-edge emission becomes broader and the relative intensity of the 1.6 eV emission to that of the band-edge emission bands tends to decrease. The 10% Cd-doped MnS NWs show the appearance of a 2.13 eV emission band, which can be assigned to the d–d ( $^4\text{T}_1 \rightarrow ^6\text{A}_1$ ) transition of the  $\text{Mn}^{2+}$  ions at the tetrahedral sites.<sup>30</sup> The time-resolved PL spectrum of the  $\text{Mn}^{2+}$  emission (1.6 eV) at 7 K, excited by 266 nm (4.66 eV) radiation, is displayed in the insets. The fitting of the rise and decay parts with a biexponential function provides average decay times of 40 and 30 μs for the MnS NWs and 10% Cd-doped MnS NWs, respectively, showing a decrease with increasing Cd content. These values remain nearly the same until 100 K, thereby providing the lifetime of the  $\text{Mn}^{2+}$  excited states at the defect sites.

Mochizuki and Takayama suggested that the 1.6 eV emission band originating from the decay of the  $\text{Mn}^{2+}$  excitons is closely related to the impurity-perturbed states of the  $\text{Mn}^{2+}$  ions and that its appearance at the low temperatures (below 150 K) might be correlated with the antiferromagnetic spin-ordering ( $T_N = 150$  K for the bulk); the energy transfer rate between the neighboring  $\text{Mn}^{2+}$  ions is smaller in the spin-ordered than in the paramagnetic phase.<sup>17</sup> Geode et al. reported that the  $T_N$  of the Cd-doped MnS bulk decreases with increasing Cd content: 152 K for MnS, 127 K for 10% Cd-doped MnS, and 105 K for 20% Cd.<sup>15</sup> They also measured the effective decay time (defined as the decay time corresponding to  $1/10$  of the initial intensity) for the bulk MnS and Cd-doped MnS:  $\tau = 140$  μs for MnS and  $\tau = 60$  μs for  $\text{Mn}_{0.8}\text{Cd}_{0.2}\text{S}$ .<sup>16</sup> They concluded that the energy transfer between neighboring  $\text{Mn}^{2+}$  ions is influenced by the antiferromagnetic spin-ordering.

Consistent with these previous studies, the antiferromagnetic spin-ordering of the MnS NWs might be responsible for the vanishing of the  $\text{Mn}^{2+}$  emission band at high temperatures and the variation of the intensity and decay time of the  $\text{Mn}^{2+}$  emission band depending on the Cd content. The incorporation of diamagnetic  $\text{Cd}^{2+}$  ions at the lattice sites results in missing spins, which causes the antiferromagnetic ordering of the  $\text{Mn}^{2+}$  ions to deviate from its normal behavior. The resulting less ordered magnetic interaction should significantly quench the  $\text{Mn}^{2+}$  excited states to other shallow bound states, with the result that the intensity and decay time decrease with increasing Cd content. The decay times of the NWs are within the same time scale as that of the bulk. However, the somewhat shorter decay time of the NWs than that of the bulk could be caused by the surface effect of the nanosize structures; the lattice disorders

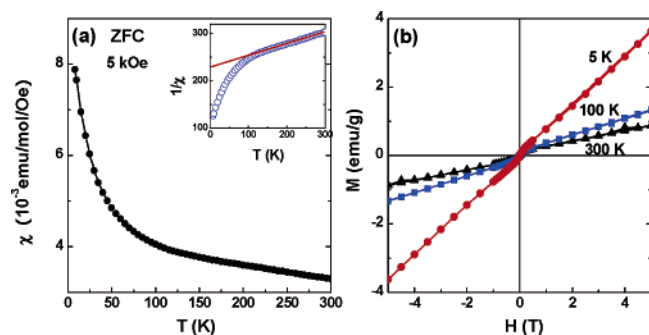


**Figure 5.** (a) Temperature-dependent zero-field cooled (ZFC) magnetic susceptibility ( $\chi$ ) measured with  $H = 5$  kOe. The inset represents the corresponding  $1/\chi$  data with a linear fit extrapolated to  $T = 0$ . (b) The  $M$  (emu/g) versus  $H$  curves at 5, 100, and 300 K.

associated with the enhanced surface area would accelerate the nonradiative energy relaxation rate of the excited  $\text{Mn}^{2+}$  states into other states. The broadening of the band edge emission and the production of the tetrahedral  $\text{Mn}^{2+}$  ion sites in the case of the 10%-Cd doped MnS NWs can certainly be ascribed to the enhanced lattice disorders induced by the higher concentration of Cd doping. To study the correlation between the PL properties and the antiferromagnetic ordering in more detail, we measured the magnetic properties of the MnS NWs.

In Figure 5a we plot the temperature dependence of the zero-field-cooled (ZFC) magnetic susceptibility ( $\chi$ ) measured at 5 kOe for the MnS NWs. We collected 5 mg of the MnS NWs by scraping them off from a number of substrates grown under the same growth conditions, using a nonmagnetic knife. The plot of the inverse of the magnetic susceptibility as a function of temperature shows that the magnetization is linear in the higher temperature part (above  $\sim 100$  K) but deviates from the linear fit in the lower temperature. The higher temperature linear part obeys the Curie–Weiss law,  $M/H = C/(T - \theta_p)$ , where  $C$  is the Curie constant and  $\theta_p$  the paramagnetic Curie temperature (inset). From the extrapolation,  $\theta_p = -903$  K is obtained, indicating that the magnetic interactions between the  $\text{Mn}^{2+}$  ions are antiferromagnetic in nature (inset). From the slope, we obtain the effective magnetic moment  $\mu_{\text{eff}} = 5.64 \mu_B$ , where  $\mu_B$  is the Bohr magneton. This is slightly lower than the value ( $5.9 \mu_B$ ) of a free  $\text{Mn}^{2+}$  ion but is comparable with the value ( $5.6 \mu_B$ ) of bulk MnS.<sup>6</sup> We further studied the field effect on the magnetic phase by measuring the  $M(H)$  values at 5, 100, and 300 K (Figure 5b). The magnetization is linear in fields higher than 1 T, but deviates from the linear fit in fields below 5 kOe, displaying an S-shaped feature without hysteresis. This result is quite consistent with the susceptibility data, indicating the signature of the antiferromagnetic state. Therefore, the appearance of the 1.6 eV emission band at the lower temperatures ( $< 150$  K) would be explained by such antiferromagnetic ordering of  $\text{Mn}^{2+}$  ions.

Kan et al. reported that as the size of  $\alpha$ -MnS nanoparticles decreases from 80 to 20 nm, their  $T_N$  value decreases from 116 to 50 K.<sup>24</sup> Jun et al reported that 2.2-nm-diameter  $\alpha$ -MnS NWs (length of  $\sim 176$  nm) and 2.5-nm nanocubes exhibit antiferromagnetic behavior with  $T_N = 30$  and 18 K, respectively.<sup>26</sup> These results imply that the magnetic properties of MnS nanostructures are strongly dependent on their size and dimension. Therefore, the present result that the  $\alpha$ -MnS NWs exhibit no obvious spin-ordering temperature, despite their antiferromagnetic interaction, may be coherent with these previous observations. The  $\theta_p$  value of the MnS NWs is higher than that ( $\theta_p = -490$  K) of the bulk MnS<sup>6</sup> and that ( $\theta_p = -174$  K) of the 80-nm nanoparticles.<sup>24</sup> This remarkably stronger antiferromagnetic correlation of the

NWs may also be associated with the intrinsic anisotropic geometry of the NW morphology. On the other hand, there is also the possibility that these unique paramagnetic properties of the MnS NWs may originate from the  $\text{Cd}^{2+}$  impurity ( $< 1\%$ ), whose content is below the detection limit of XPS. The incorporation of a trace amount of diamagnetic  $\text{Cd}^{2+}$  ions can induce more paramagnetic behaviors. It could also rationalize the difference between the decay times of the MnS NWs (40  $\mu\text{s}$ ) and MnS bulk (140  $\mu\text{s}$ ). Although the magnetizations of the 5 and 10% Cd-doped MnS NWs have not yet been measured (they are currently under investigation), it is expected that the magnitude of this antiferromagnetic interaction would be reduced as the Cd content increases.

For the sake of comparison, we measured the magnetic properties of  $\alpha$ -MnS (Aldrich, 99.9%) powders and found that  $T_N = 154$  K (Supporting Information, Figure S1). The temperature-dependent XRD pattern shows the discontinuous contraction (probably rhombohedral or trigonal distortion) of the lattice constants near 150 K, accompanying the antiferromagnetic spin-ordering (Supporting Information, Figure S2).<sup>11,12</sup> However, there is no clear transition of the lattice constants for the MnS NWs. This provides evidence that the MnS NWs have more pronounced paramagnetic properties than the bulk.

#### 4. Conclusions

High-yield Cd-doped MnS NWs were synthesized by the CVD of  $\text{MnCl}_2/\text{CdS}$ . Their diameter was in the range of 50–80 nm. They consisted of single-crystalline cubic  $\alpha$ -MnS crystals, uniformly grown with the [110] direction parallel to the long axis. Their Cd content, 5 and 10%, was controlled by adjusting the temperature (600–700 °C) of the Mn source during the synthesis. The EDX line-scan and XPS data reveal that the 5 and 10% Cd contents are homogeneously doped over the cross section of the MnS NWs. The XRD pattern confirms the presence of the rock-salt  $\alpha$ -MnS phase for all of the Cd-doped MnS NWs. The peak position is shifted to a lower angle, indicating that the Cd doping expands the lattice constants of  $\alpha$ -MnS crystal. Ten percent Cd doping increases the lattice constants by 0.3%. The temperature-dependent PL spectra show that as the Cd dopant is incorporated into the lattice, the band-edge emission band at 2.9 eV becomes broader and the intensity of the  $\text{Mn}^{2+}$  emission band at 1.6 eV, which appears at temperatures below  $\sim 150$  K, is much reduced. As the Cd content increases from 0 to 10%, the decay times of the 1.6 eV emission decreases from 40 to 30  $\mu\text{s}$ . These results could be explained by the reduced antiferromagnetic interaction between the  $\text{Mn}^{2+}$  ions by incorporation of diamagnetic  $\text{Cd}^{2+}$  ions. The magnetization measurement indicates that the MnS NWs are paramagnetic with antiferromagnetic interactions, which is different from the properties of the antiferromagnetic MnS bulk phase ( $T_N = \sim 150$  K). We suggest that these unique magnetic properties could be closely related to the anisotropic NW geometry or the Cd impurity.

**Acknowledgment.** This work was supported by the Korea Research Foundation (Project Nos. R14-2003-033-01003-0; 2003-015-C00265; R02-2004-000-10025-0). The SEM, HVEM, and SQUID measurements were performed at the Korea Basic Science Institute. The experiments at PLS were supported in part by MOST and in part by POSTECH.

**Supporting Information Available:** Figures showing temperature-dependent ZPC and FC magnetic susceptibility of the MnS powders and temperature-dependent XRD (200) and (220)

peaks of MnS powders. This material is available free of charge via the Internet at <http://pubs.acs.org>.

## References and Notes

- (1) Hu, J.; Odom, T. W.; Lieber, C. M. *Acc. Chem. Res.* **1999**, *32*, 435.
- (2) Gudiksen, M. S.; Lauhon, L. J.; Wang, J.; Smith, D. C.; Lieber, C. M. *Nature (London)* **2002**, *415*, 617.
- (3) Duan, X.; Huang, Y.; Agarwal, R.; Lieber, C. M. *Nature (London)* **2003**, *421*, 241.
- (4) Huang, Y.; Duan, X.; Lieber, C. M. *Small* **2005**, *1*, 142.
- (5) Huffman, D. R.; Wild, R. L. *Phys. Rev.* **1967**, *156*, 989.
- (6) Banewicz, J. J.; Lindsay, R. *Phys. Rev.* **1956**, *104*, 318.
- (7) Corliss, L.; Elliot, N.; Hastings, J. *Phys. Rev.* **1956**, *104*, 924.
- (8) Lindsay, R.; Banewicz, J. J. *Phys. Rev.* **1958**, *110*, 634.
- (9) Lines, M. E.; Jones, E. D. *Phys. Rev.* **1966**, *141*, 525.
- (10) Huffman, D. R.; Wild, R. L. *Phys. Rev.* **1966**, *148*, 526.
- (11) Morosin, B. *Phys. Rev. B* **1970**, *1*, 236.
- (12) Heikens, H. H.; Wiegers, G. A.; van Bruggen, C. F. *Solid State Commun.* **1977**, *24*, 205.
- (13) Terasawa, H.; Kambara, T.; Gondaira, T.; Teranishi, T.; Sato, K. *J. Phys. C: Solid St. Phys.* **1980**, *13*, 5615.
- (14) Goede, O.; Hemibrod, H.; Weinhold, V. *Phys. Status Solidi B* **1986**, *136*, K49.
- (15) Goede, O.; Backs, W.; Hemibrod, H.; Kanis, M. *Phys. Status Solidi B* **1989**, *151*, 311.
- (16) Hemibrod, H.; Benecke, C.; Goede, O.; Gumlich, H.-E. *J. Cryst. Growth* **1990**, *101*, 911.
- (17) Mochizuki, S.; Takayama, N. *J. Phys.: Condens. Matter* **1991**, *3*, 2729.
- (18) Aplestin, S. S.; Ryabinkina, L. I.; Abramova, G. M.; Romanova, O. B.; Kiselev, N. I.; Bovina, A. F. *Phys. Sol. Stat.* **2004**, *46*, 2067.
- (19) Kennedy, S. W.; Harris, K.; Summerville, E. *J. Sol. State Chem.* **1980**, *31*, 355.
- (20) Goede, O.; Hemibrod, H.; Weinhold, V.; Schnürer, E.; Eberle, H. *G. Phys. Status Solidi (b)* **1987**, *143*, 511.
- (21) Hastings, J. M.; Corliss, L. M.; Kunnmann, W.; Mukamel, D. *Phys. Rev. B* **1991**, *24*, 1388.
- (22) Wei, S.-H.; Zunger, A. *Phys. Rev. B* **1993**, *48*, 6111.
- (23) Shromme, B. J.; Zhang, Y.; Smith, D. J. Sivananthan, S. *Appl. Phys. Lett.* **1995**, *67*, 2690.
- (24) Kan, S.; Felner, I.; Banin, U. *Isr. J. Chem.* **2001**, *41*, 55.
- (25) Lu, J.; Qi, P.; Peng, Y.; Meng, Z.; Yang, Z.; Yu, W.; Qian, Y. *Chem. Mater.* **2001**, *13*, 2169.
- (26) Jun, Y.; Jung, Y.; Cheon, J. *J. Am. Chem. Soc.* **2002**, *124*, 615.
- (27) Joo, J.; Na, H. B.; Yu, T.; Yu, J. H.; Kim, Y. W.; Wu, F.; Zhang, J. Z.; Hyeon, T. *J. Am. Chem. Soc.* **2003**, *125*, 11100.
- (28) Lei, S.; Tang, K.; Yang, Q.; Zheng, H. *Eur. J. Inorg. Chem.* **2005**, 4124.
- (29) Pradhan, N.; Katz, B.; Efrima, S. *J. Phys. Chem. B* **2003**, *107*, 13843.
- (30) Yang, P.; Lü, M.; Song, C.; Gu, F.; Liu, S.; Xu, D.; Yuan, D.; Cheng, X. *J. Non-Cryst. Sol.* **2002**, *311*, 99.
- (31) An, C.; Tang, K.; Liu, X.; Li, F.; Zhou, G.; Qian, Y. *J. Cryst. Growth* **2003**, *252*, 575.
- (32) Ge, J.; Li, Y. *Chem. Commun.* **2003**, *13*, 2498.
- (33) Ge, J.-P.; Wang, J.; Zhang, H.-X.; Zheng, H.; Li, Y.-D. *Chem.—Eur. J.* **2004**, *10*, 3525.
- (34) Na, C. W.; Han, D. S.; Kim, D. S.; Kang, Y. J.; Lee, J. Y.; Park, J.; Oh, D. K.; Kim, K. S.; Kim, D. *J. Phys. Chem. B* **2006**, *110*, 6699.